



Supplementary Information for

Evolutionary Design of Magnetic Soft Continuum Robots

Liu Wang^{1,2}, Dongchang Zheng¹, Pablo Harker³, Aman B. Patel³, Chuan Fei Guo², Xuanhe Zhao^{1,4*}

¹Department of Mechanical Engineering, Massachusetts Institute of Technology, Cambridge, MA 02139, USA

²Department of Materials Science and Engineering, Southern University of Science and Technology, Shenzhen 518055, China

³Department of Neurosurgery, Massachusetts General Hospital and Harvard Medical School, Boston, MA 02149, USA

⁴Department of Civil and Environmental Engineering, Massachusetts Institute of Technology, Cambridge, MA 02139, USA

*Corresponding author: Xuanhe Zhao

Email: zhaox@mit.edu

This PDF file includes

Supplementary text

Table S1

Figure. S1 to S11

Legend for Movie S1

SI References

Section S1: Analytical solutions for MSCRs with a uniform particle concentration

Consider a distal portion with a uniform particle volume fraction (ϕ) lying along the x -axis in the reference configuration. The magnetization vector can be represented as $\mathbf{M} = M_0\phi\mathbf{e}_x$ where M_0 denotes the magnetization strength. The shear modulus of the distal portion is $G = G_0f(\phi)$ where $f(\phi) = \exp[2.5\phi/(1 - 1.35\phi)]$. When a uniform actuation magnetic field is applied at an angle φ with respect to the reference configuration (i.e., $\mathbf{B} = B\cos\varphi\mathbf{e}_x + B\sin\varphi\mathbf{e}_y$), the governing equation in Eq. 1 can be written as

$$EI\kappa(s) = \int_s^L \tau^{\text{magnetic}} A ds = \int_s^L M_0 B A \phi \sin(\varphi - \theta) ds \quad [\text{S1}]$$

Differentiating both sides of Eq. S1 and rearranging gives

$$\frac{d^2\theta}{ds^2} + Q \sin(\varphi - \theta) = 0 \quad [\text{S2}]$$

where the coefficient $Q = \frac{16 M_0 B \phi}{3 G_0 D^2 f(\phi)}$ in which D is the cross-sectional diameter. With the help of chain rule, Eq. S2 can be expressed in the following integral form:

$$\int \frac{d^2\theta}{ds^2} \frac{d\theta}{ds} ds = - \int Q \sin(\varphi - \theta) ds \quad [\text{S3}]$$

which upon integration yields

$$\frac{1}{2} \left(\frac{d\theta}{ds} \right)^2 = -Q \cos(\varphi - \theta) + C \quad [\text{S4}]$$

The constant C can be determined from the boundary condition that there is no bending moment at the free tip, i.e., $\theta'(L) = 0$, which leads to

$$C = Q \cos(\varphi - \theta_L) \quad [\text{S5}]$$

where θ_L denotes the bending angle of the free tip in the deformed configuration. Then Eq. S4 can be rearranged as

$$ds = \sqrt{\frac{1}{2Q} \frac{d\theta}{\sqrt{\cos(\varphi - \theta_L) - \cos(\varphi - \theta)}}} \quad [\text{S6}]$$

Integrating Eq. S6 produces the expression for the total length of the elastica,

$$L = \sqrt{\frac{1}{2Q}} \int_0^{\theta_L} \frac{d\theta}{\sqrt{\cos(\varphi - \theta_L) - \cos(\varphi - \theta)}} = \sqrt{\frac{1}{2Q}} \Phi(\varphi, \theta_L) \quad [\text{S7}]$$

where nondimensional function $\Phi(\varphi, \theta_L)$ is defined as

$$\Phi(\varphi, \theta_L) = \int_0^{\theta_L} \frac{d\theta}{\sqrt{\cos(\varphi - \theta_L) - \cos(\varphi - \theta)}} = \frac{2}{\sqrt{\cos(\varphi - \theta_L) - 1}} \left[F\left(\frac{\varphi - \theta_L}{2}, \csc\frac{\varphi - \theta_L}{2}\right) - F\left(\frac{\varphi}{2}, \csc\frac{\varphi - \theta_L}{2}\right) \right] \quad [\text{S8}]$$

with the function F denoting the incomplete elliptic integral of the first kind defined as

$$F(\alpha, k) = \int_0^\alpha \frac{d\theta}{\sqrt{1 - k^2 \sin^2 \theta}} \quad [\text{S9}]$$

Then, Eq. S7 can be rewritten as

$$\frac{16 M_0 B L^2 \phi}{3 G_0 D^2 f(\phi)} = \frac{1}{2} \Phi^2(\varphi, \theta_L) \quad [\text{S10}]$$

Therefore, θ_L can be solved from Eq. S10. The kinematic relation of the infinitesimal arc length ds reads as

$$\begin{aligned} dx &= ds \cos \theta = \sqrt{\frac{1}{2Q} \frac{\cos \theta d\theta}{\sqrt{\cos(\varphi - \theta_L) - \cos(\varphi - \theta)}}} \\ dy &= ds \sin \theta = \sqrt{\frac{1}{2Q} \frac{\sin \theta d\theta}{\sqrt{\cos(\varphi - \theta_L) - \cos(\varphi - \theta)}}} \end{aligned} \quad [\text{S11}]$$

By plugging θ_L into Eq. S11, one can solve the Cartesian coordinates of the tip by integrating from 0 to L , i.e.,

$$\begin{aligned} x_L &= \int_0^L dx = \int_0^{\theta_L} \sqrt{\frac{1}{2Q} \frac{\cos \theta d\theta}{\sqrt{\cos(\varphi - \theta_L) - \cos(\varphi - \theta)}}} \\ y_L &= \int_0^L dy = \int_0^{\theta_L} \sqrt{\frac{1}{2Q} \frac{\sin \theta d\theta}{\sqrt{\cos(\varphi - \theta_L) - \cos(\varphi - \theta)}}} \end{aligned} \quad [\text{S12}]$$

Section S2: Optimization of MSCRs using the genetic algorithm

The optimization of MSCR with the genetic algorithm was performed using Matlab 2020a. We randomly generated the first generation of 100 MSCRs by assigning a random ϕ between 0 and 0.4 to each voxel of each MSCR. Then we calculated the workspaces of the 100 MSCRs in the first generation using the developed finite difference method. Thereafter, we selected 100 MSCRs from the first generation based on the stochastic universal sampling method (1). In the stochastic universal sampling, we first ranked the workspaces of 100 MSCRs from high to low and mapped them to contiguous segments of a line in which each segment is equal in size to its workspace. Then the total length of the line equals the sum of all workspaces, denoted as W . Next, we randomly generated 100 evenly-spaced points with an interval of $W/100$ on the line and select 100 MSCRs in whose segment the point lies (**Fig. S4**). MSCRs with a larger workspace can be selected multiple times while MSCRs with a lower workspace may not be selected. Then the second generation of 100 MSCRs was generated by 5% elitism, 85% crossover, and 10% mutation. In the 5% elitism, 5 MSCRs with the largest workspaces propagated to the second generation without changing their polarity patterns. In the 85% crossover, we randomly swapped some voxels of two selected MSCRs. In the 10% mutation, we randomly altered some voxels of the MSCR to a different value between 0 and 0.4. This evolutionary process was repeated over multiple generations until the difference between the largest workspace and the mean value of all workspaces in a certain generation of MSCRs is smaller than the tolerance (10^{-3}).

Section S3: Analytical solutions for MSCRs with a permanent-magnet tip

Schematic of the distal portion with a permanent magnet at the tip is given in **Fig. S7** in which the length of the magnet is denoted as L_1 . The non-magnetized part, i.e., the polymer in $0 \leq s \leq L_1$, has shear modulus $G = G_0$. As the modulus of the magnet (\sim GPa) is much larger than the polymer, it can be treated as a rigid body. The magnetization of the magnet is constant $\mathbf{M} = M_0 \mathbf{e}_x$ in the reference configuration. In

the deformed configuration, the bending angle of the tip is denoted as θ_L . Then for the non-magnetized portion from 0 to $L - L_1$, it is subject to a constant bending moment $\Gamma(s)$ at equilibrium,

$$\Gamma(s) = \int_{L_1}^L \tau^{\text{magnetic}} A ds = M_0 B A L_1 \sin(\varphi - \theta_L) \quad [\text{S13}]$$

Then the governing equation Eq. 1 can be written as

$$EI\kappa(s) = M_0 B A L_1 \sin(\varphi - \theta_L) \quad [\text{S14}]$$

Eq. S14 suggests that the deformed elastica of the non-magnetized part $0 \leq s < L - L_1$ has a constant curvature

$$\kappa(s) \equiv \frac{d\theta}{ds} = \frac{M_0 B A L_1}{EI} \sin(\varphi - \theta_L) \quad [\text{S15}]$$

from which we can find θ_L

$$\theta_L = \frac{M_0 B A L_1 (L - L_1)}{EI} \sin(\varphi - \theta_L) \quad [\text{S16}]$$

Therefore, Eq. S15 can be simplified as

$$ds = \frac{L - L_1}{\theta_L} d\theta \quad [\text{S17}]$$

Then the kinematic relation reads as


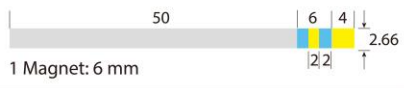

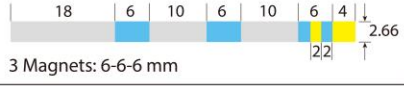

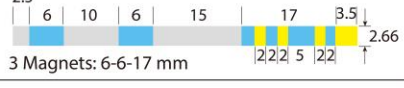

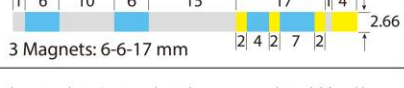

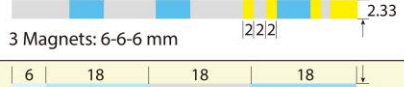

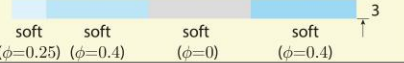
$$\begin{aligned} dx &= ds \cos \theta = \frac{L - L_1}{\theta_L} \cos \theta d\theta \\ dy &= ds \sin \theta = \frac{L - L_1}{\theta_L} \sin \theta d\theta \end{aligned} \quad [\text{S18}]$$

The Cartesian coordinates of the magnet tip are given

$$\begin{aligned} x_L &= \int_0^{L-L_1} dx + L_1 \cos \theta_L = (L - L_1) \frac{\sin \theta_L}{\theta_L} + L_1 \cos \theta_L \\ y_L &= \int_0^{L-L_1} dy + L_1 \sin \theta_L = (L - L_1) \frac{(1 - \cos \theta_L)}{\theta_L} + L_1 \sin \theta_L \end{aligned} \quad [\text{S19}]$$

Eq. S19 shows that, for a specific magnet length L_1 , the tip deflection depends only on the tip bending angle θ_L . By tuning the actuation magnetic field, the tip bending angle can be achieved from 0 to 180°, thus all the tip trajectories fall on a master curve rather than enveloping an area. Therefore, the half workspace is a curve with a zero area. The theoretical solutions, in comparison with FEM results, has been validated by experiments (**Fig. S11**).

Table S1. Comparison between the optimized magnetic soft continuum robot and five commercial catheters with embedded magnets

Product Model	Picture	Schematic* (mm)	Normalized Half Workspace	Reference
Helios I with 1 magnet (Stereotaxis, USA)		 <p>1 Magnet: 6 mm</p>	0	[1]
Helios II with 3 magnets (Stereotaxis, USA)		 <p>3 Magnets: 6-6-6 mm</p>	0.065	[1]
Thermocool RMT with 3 magnets (Biosense Webster, USA)		 <p>3 Magnets: 6-6-17 mm</p>	0.18	[2][3]
Navistar RMT with 3 magnets (Biosense Webster, USA)		 <p>3 Magnets: 6-6-17 mm</p>	0.17	[2]
Trignum Flux G with 3 magnets (Biotronik, Germany)		 <p>3 Magnets: 6-6-6 mm</p>	0.13	[4] [5]
Magnetic Soft Continuum Robot		 <p>soft ($\phi=0.25$) soft ($\phi=0.4$) soft ($\phi=0$) soft ($\phi=0.4$)</p>	0.27	This work

* Total length is chosen as 60 mm for consistent comparison.

** Electrodes are regarded as the polymer matrix in the calculation of the workspace.

[1] Chun et al (2007), European Heart Journal, 28, 190-195;

[2] Biosense Webster Product Catalog (2020);

[3] Chun et al (2010), Circulation: Arrhythmia and Electrophysiology, 3(5), 458-464;

[4] Biotronik Product Catalog/Electrophysiology;

[5] Le, V. T. (2015). Doctoral Thesis. Edith Cowan University. <https://ro.ecu.edu.au/theses/1711>

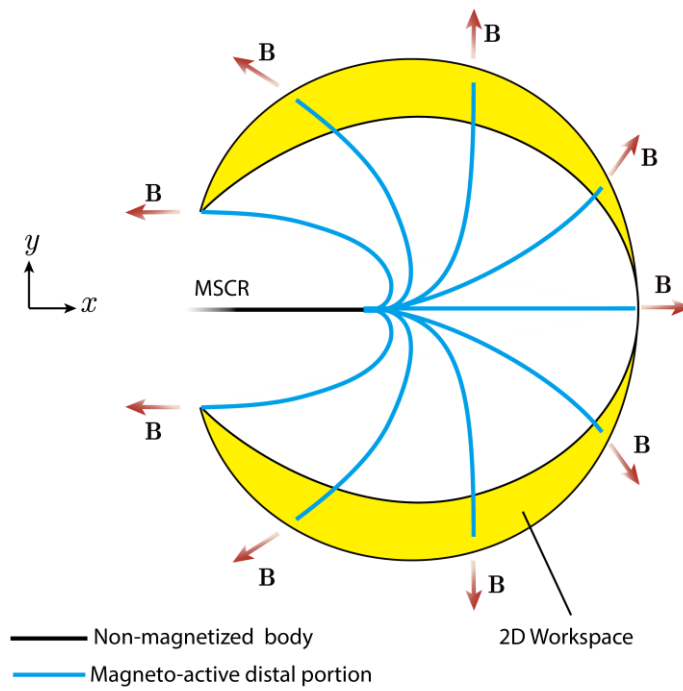


Fig S1. The 2D workspace of the MSCR is achieved under uniform magnetic fields up to 40 mT applied along various directions in a plane. The workspace is symmetric about the undeformed axis of the MSCR (i.e., x -axis).

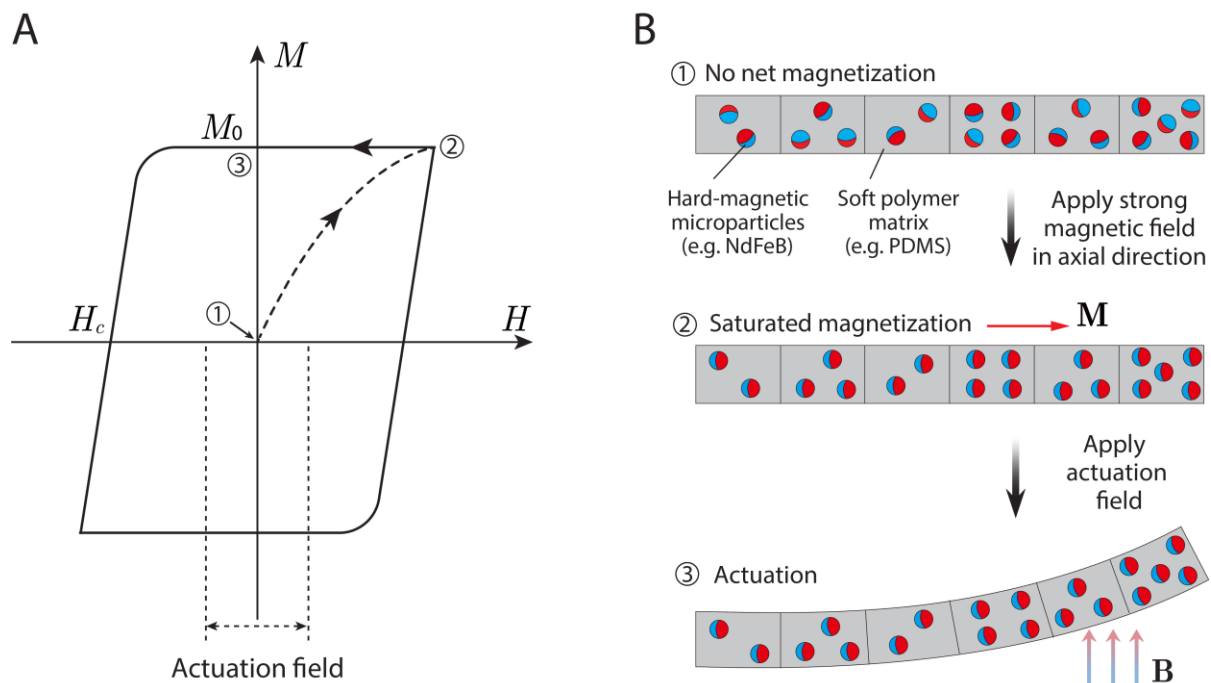


Fig. S2. (A) Magnetization curve and hysteresis loops of hard-magnetic materials. The curves show the magnetization (M) as a function of the applied magnetic field strength (H). Hard-magnetic materials maintain the remanent magnetization (M_0) when the actuation field strength is much smaller than the coercivity (H_c). (B) Schematic illustration of the MSCR with programmed remanent magnetization resulting from the aligned hard-magnetic particles with intrinsic dipoles in the polymer matrix. Adopted from ref (2)

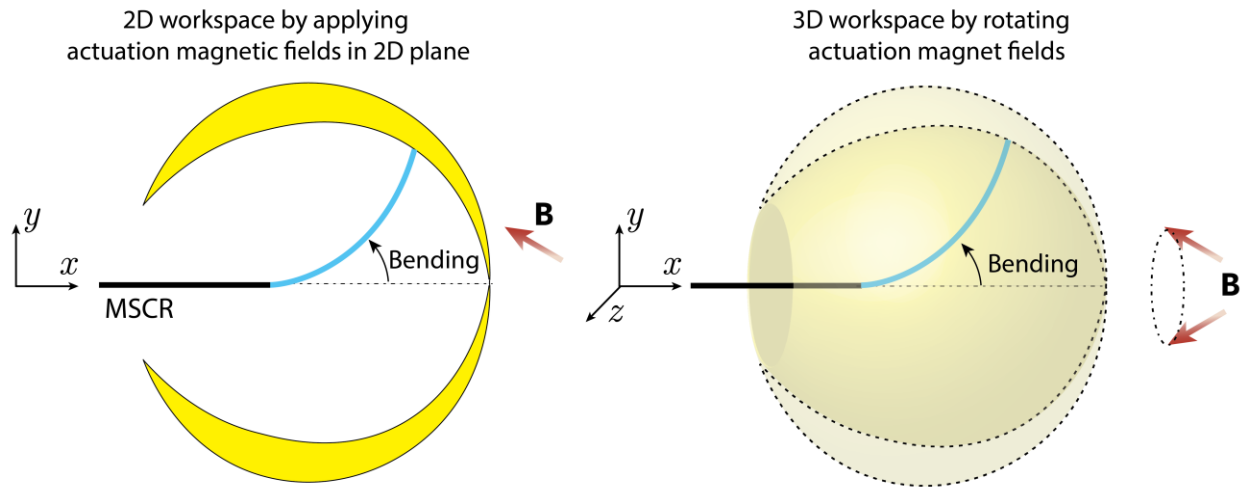


Fig S3. The 2D workspace of the MSCR is achieved under uniform magnetic fields up to 40 mT applied along various directions in a plane. Rotating the actuation magnetic field around the axis of the undeformed MSCR will give a 3D workspace which is a revolution of the 2D workspace.

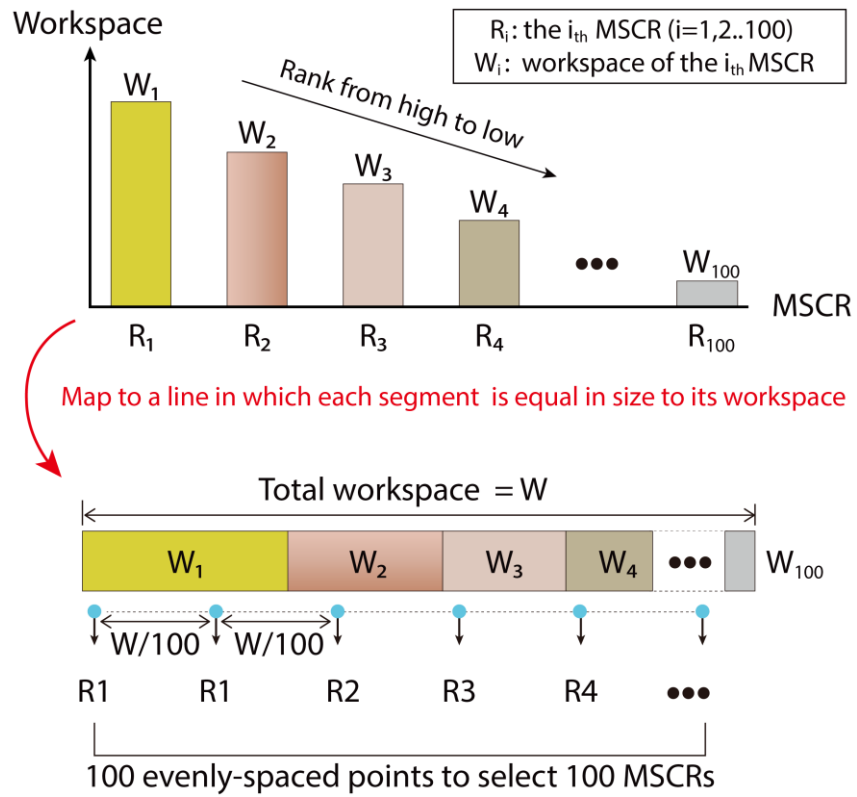


Fig. S4. Schematic illustration of the stochastic universal sampling. 100 MSCRs, labeled as R_1, R_2, \dots, R_{100} , are ranked by their workspaces, denoted as W_1, W_2, \dots, W_{100} , from high to low and are mapped to a line in which each segment is equal in size to its workspace. 100 evenly-spaced points are used to select 100 MSCRs in whose segment the point lies.

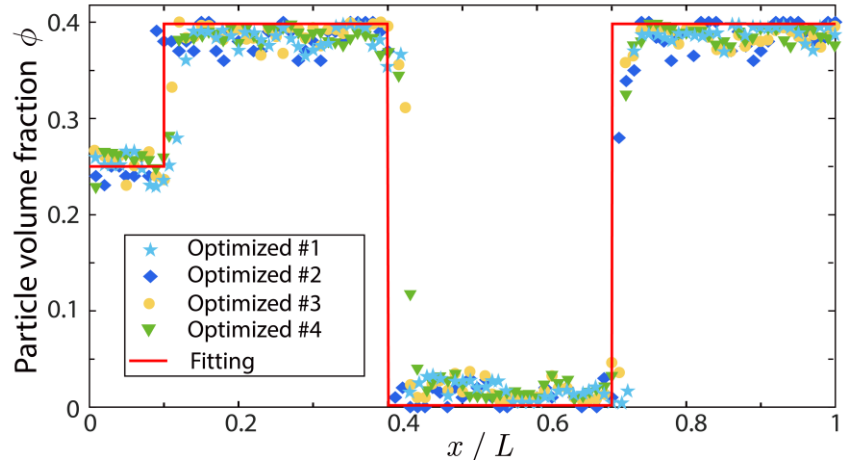


Fig S5. The hard-magnetic particle distribution (markers) and its fitted function (red line) of the optimized MSCR. Genetic algorithm optimizations with different initializations yield the same fitted results.

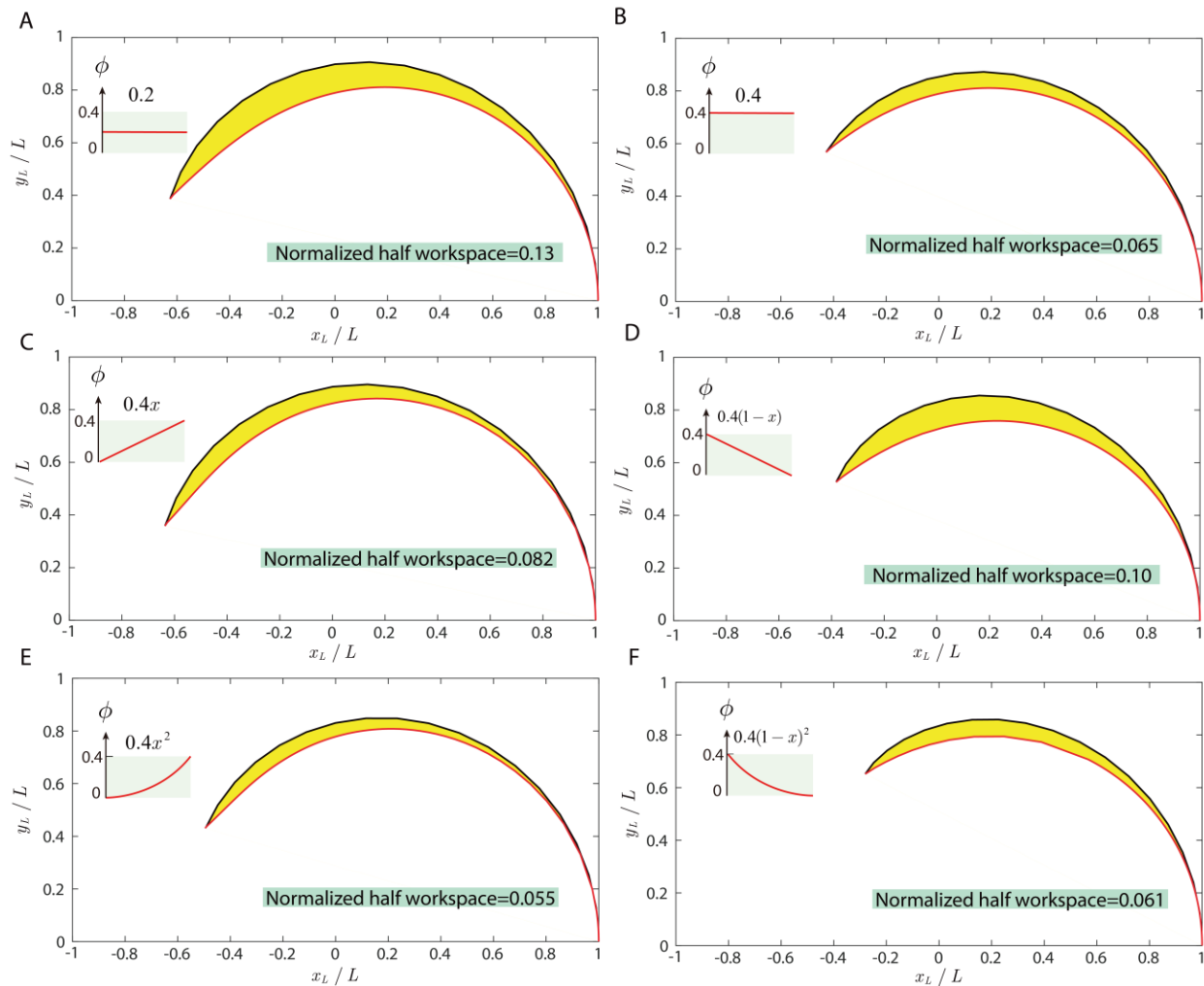


Fig. S6 The normalized half workspace of MSCRs by dispersing hard-magnetic particles in polymer matrices. Magnetic particle distribution: (A) constant $\phi = 0.2$; (B) constant $\phi = 0.4$; (C) linearly increasing from 0 to 0.4; (D) linearly decreasing from 0.4 to 0; (E) parabolically increasing form 0 to 0.4; (F) parabolically decreasing from 0.4 to 0.

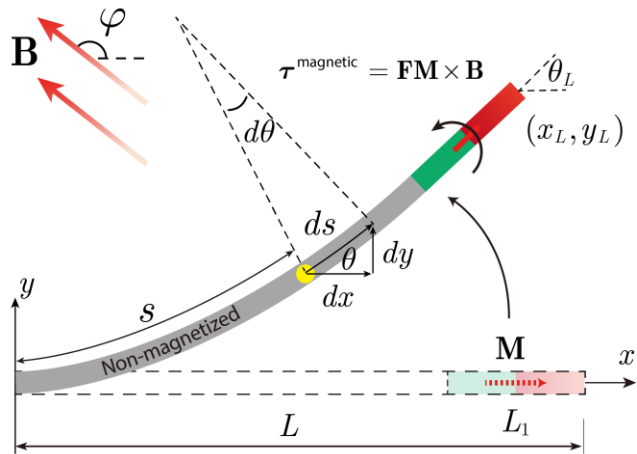


Fig. S7. Schematic illustration of the distal portion with a permanent magnet at the tip. The permanent magnet is treated as a rigid body with length and rotation angle denoted L_1 and θ_L , respectively.

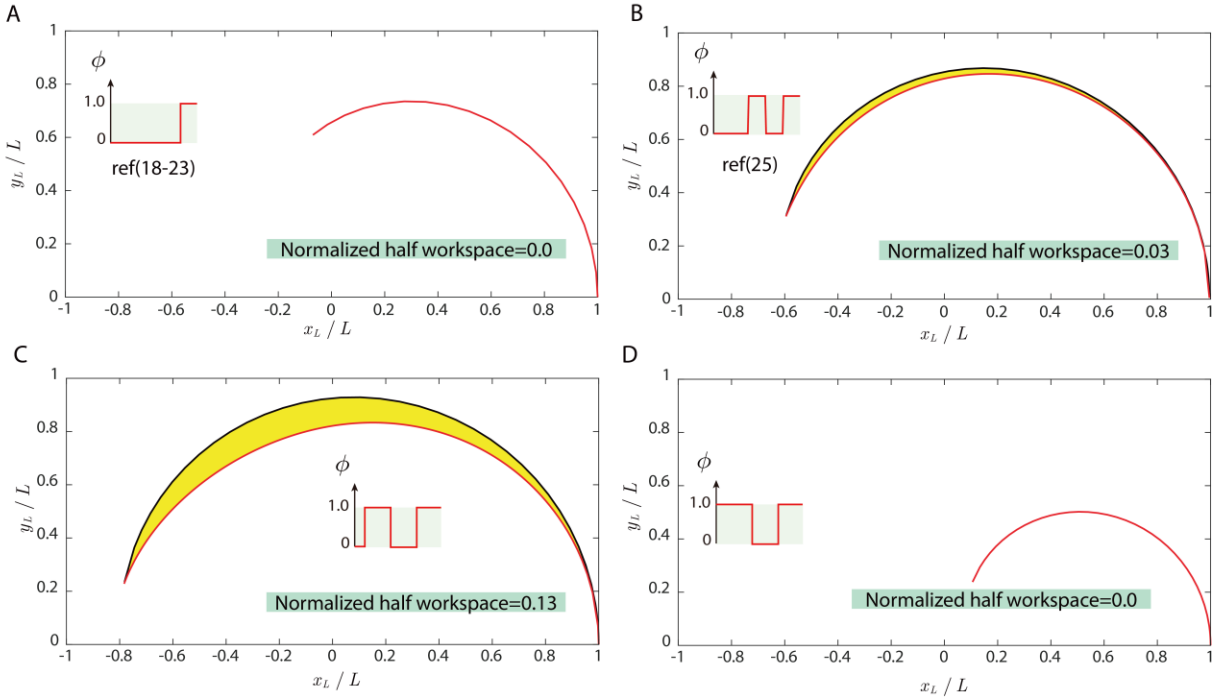


Fig. S8 The normalized half workspace of MSCRs by embedding permanent magnets into elastomer. (A) A representative MSCR with a permanent magnet at the distal tip. Towards the distal tip of the MSCR, the polarity pattern is $\phi = [0,0,0,0,0,0,0,0,1]$; (B) A MSCR with two permanent magnets with polarity pattern $\phi = [0,0,0,0,1,1,0,0,1,1]$. (C) A MSCR by changing the voxels with $\phi = 0.4$ and $\phi = 0.25$ in the optimized design into permanent magnets ($\phi = 1$) and elastomer ($\phi = 0$), respectively. The polarity pattern is $\phi = [0,1,1,1,0,0,0,1,1,1]$; (D) A MSCR by changing the voxels with $\phi = 0.4$ and $\phi = 0.25$ in the optimized design into permanent magnets ($\phi = 1$). The polarity pattern is $\phi = [1,1,1,1,0,0,0,1,1,1]$.

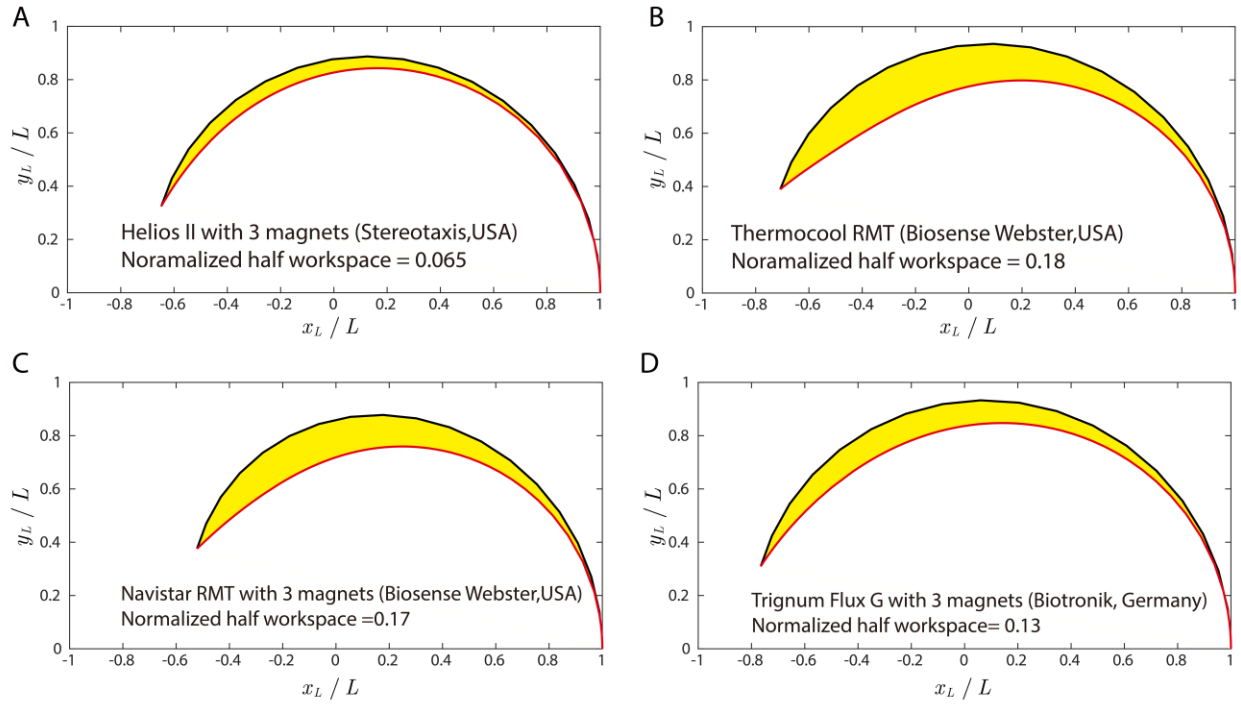


Fig. S9 The normalized half workspace of commercial magnetically-controllable catheters using 3 magnets. (A) Helios II catheter (Stereotaxis, USA); (B) Celsius RMT (Biosense Webster, USA); (C) Navistar RMT (Biosense Webster, USA); (D) Trignum Flux G (Biotronik, Germany).

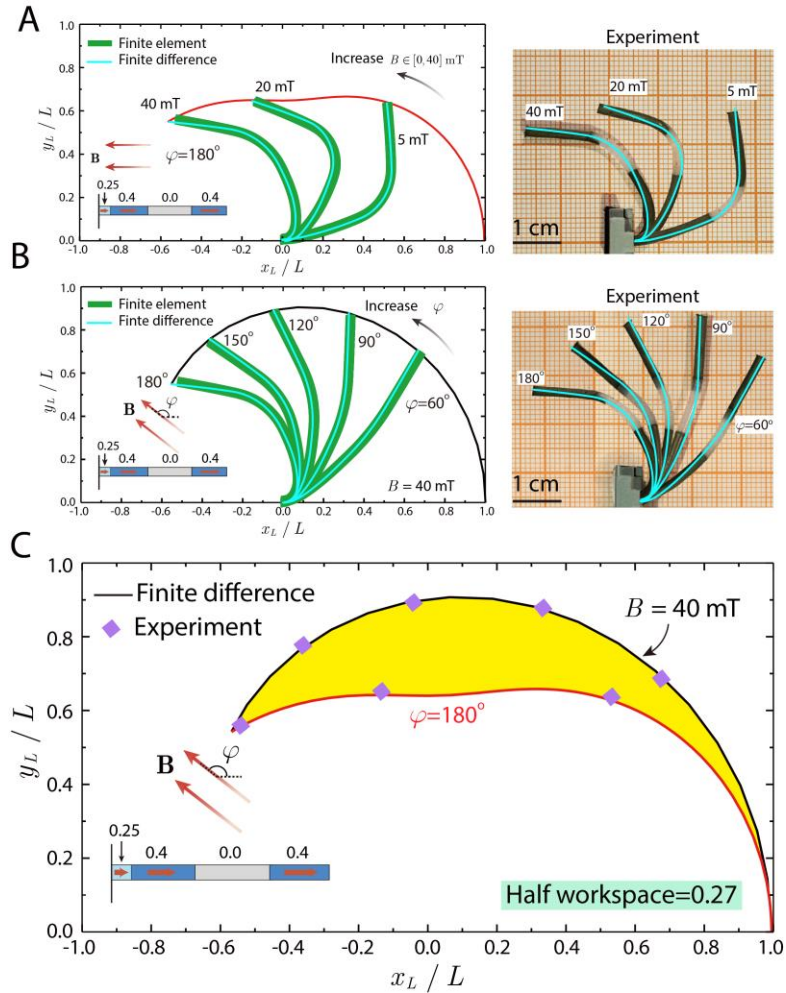


Fig. S10. Experimental validation of the optimized MSCR. (A)-(B) Comparison between the results from the finite difference method, finite element simulation, and experiments on the deformed distal portion. (A) Fixing the magnetic field angle $\varphi = 180^\circ$ while increasing the field strength up to 40 mT. (B) Fixing the magnetic field strength $B = 40$ mT while changing the field direction up to 180° . (C) Comparison of the results from the finite difference method and experiments on the normalized half workspace of the optimized MSCR.

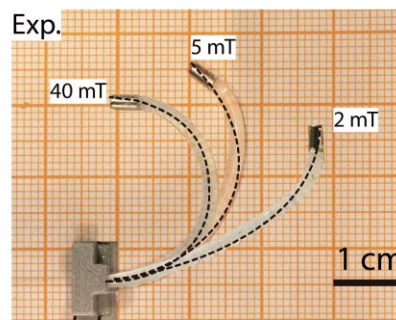
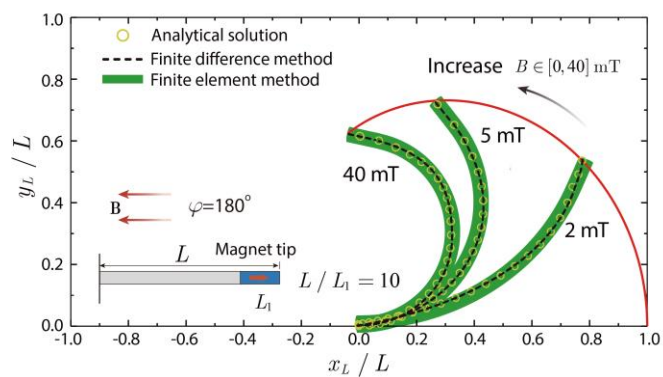


Fig. S11. Experimental validation of the workspace of a MSCR with a permanent magnet at the distal tip. The length of the permanent magnet and the distal portion is $L_1 = 4$ mm and $L = 40$ mm, respectively.

Legend for Supplementary Movie

Movie S1. Finite element simulation of the deformation of the MSCR with the optimized hard-magnetic particle distribution under actuation magnetic fields.

Reference

1. Baker JE (1987) Reducing bias and inefficiency in the selection algorithm. *Proceedings of the second international conference on genetic algorithms* pp 14-21.
2. Wang L, Kim Y, Guo CF, & Zhao X (2020) Hard-magnetic elastica. *Journal of the Mechanics and Physics of Solids* 142:104045.